Nanoscale Horizons

COMMUNICATION

View Article Online
View Journal | View Issue

Cite this: *Nanoscale Horiz.*, 2020, 5, 109

Received 4th June 2019,
Accepted 7th August 2019

DOI: 10.1039/c9nh00374f

rsc.li/nanoscale-horizons

Polyoxomolybdate (POM) nanoclusters with radiosensitizing and scintillating properties for low dose X-ray inducible radiation-radiodynamic therapy†

Debabrata Maiti,[ab] Jing Zhong,[a] Zheng Zhang,[a] Hailin Zhou,[a] Saisai Xion,[a] Ziliang Dong,[b] Sarvendra Kumar,[b] Zhuang Liu [b] and Kai Yang *[a]

In order to overcome the weak penetration of near infrared (NIR) light in photodynamic therapy (PDT), X-ray radiation (X-RT) with high deep tissue penetration could be used as a therapeutic option to completely destroy tumors. Herein, polyoxomolybdate nanoclusters (POMo NCs) with rose Bengal (RB) loading, are functionalized with chitosan (CS) and polyethylene glycol (PEG) for X-ray inducible radiation and radiodynamic therapy (X-RRDT). Our obtained POMo NCs demonstrate a strawberry shape containing 163 Mo (Mo)3 units of three edge sharing MoO_6 octahedra and connecting to the central PO_4 octahedron. Under low dose X-ray radiation, the communal effect of radiosensitization and scintillation of POMo NCs along with RB, can decrease the side effects of RT and enhance both RT and PDT efficiency. This is because the POMo NCs can not only augment RT efficacy by producing auger electrons which directly provoke DNA damage, but also enhance PDT efficacy by converting high energy X-rays into light to stimulate RB to generate singlet oxygen ($^1O_2$). *In vivo* results show that X-RRDT using POMo NCs significantly inhibits tumor growth under low dose X-ray radiation. More importantly, the as-made PEGylated POMo NCs cause no obvious side-effects to the major normal organs through histological examination. This work describes a simple strategy to design effective X-RRDT agents with multiple properties including X-ray radiosensitization, X-ray scintillation and photosensitization for X-RRDT under low dose X-ray irradiation. Our developed strategy will further promote the cancer therapeutic efficiency under low dose X-ray radiation, and bring hope for clinical cancer treatment.

New concepts

X-rays with high deep tissue penetration could be used as an excellent excited light source for enhanced photodynamic therapy (PDT), avoiding the weak penetration of near-infrared light and further improving the therapeutic efficiency of PDT. Herein, our developed polyoxomolybdate nanoclusters (POMo NCs) with the largest strawberry shape possess dual-function including X-ray triggered PDT (X-RPDT) and X-ray inducible radiation (X-RT). Under X-ray irradiation, POMo NCs could transfer high energy of X-rays into light to stimulate RB and then generate singlet oxygen for killing cancer cells. Meanwhile, the POMo NCs could also augment RT efficacy by producing auger electrons to induce DNA damage, further improving the therapeutic efficiency. We believe that the designed POMo NCs could significantly improve the therapeutic efficiency of cancer under low dose X-rays, binging hope for further cancer clinical treatment.

Compared to chemotherapy and surgery, radiotherapy (RT) using X-rays, gamma rays or an electron beam is still broadly applied for cancer treatment in clinical applications.[1] Numerous RT clinical trials have revealed that using high dose X-rays could kill most of the cancer cells, but also cause side effects to the patients.[2] Optical therapy including photodynamic therapy (PDT)[3,4] and photothermal therapy (PTT)[5,6] have been developed for the last two decades to decrease the side effects. However, the weak penetration of light limits the therapeutic efficiency of optical therapy of tumors in deeper tissue.[7] Therefore, X-rays with high deep penetration are widely used compared with NIR light. However, the side effects of RT are unavoidable. Certainly, they have been partially alleviated by advanced nano-biotechnology. During X-ray radiation therapy (X-RT), radio-sensitizers produce Compton or photoelectrons which strike adjacent water or biomolecules to generate reactive oxygen species (ROS), breaking indirectly DNA strands.[8] Owning to insufficient biomolecules near to the radiosensitizers, loss of Compton or photoelectrons is another drawback of X-RT along

[a] *State Key Laboratory of Radiation Medicine and Protection, School of Radiation Medicine and Protection & School for Radiological and Interdisciplinary Sciences (RAD-X), Collaborative Innovation Center of Radiation Medicine of Jiangsu Higher Education Institutions, Soochow University, Suzhou, Jiangsu 215123, China. E-mail: kyang@suda.edu.cn*

[b] *Institute of Functional Nano & Soft Materials (FUNSOM), & Collaborative Innovation Center of Suzhou Nano Science and Technology, Soochow University, Suzhou, Jiangsu 215123, China*

† Electronic supplementary information (ESI) available. See DOI: 10.1039/c9nh00374f

with the prime problem of side effects. Addressing the issue to minimize the side effects and to overcome the limitations of X-RT and PDT, the use of X-rays for X-ray inducible PDT (X-RDT) has become a promising technique for the treatment of malignant tumors in the last decade.[9–11] X-RDT is an energy transduction process. The scintillator nanoparticles (ScNPs) could convert the high energy X-rays into light to stimulate photosensitizers (PS) for generation of toxic reactive oxygen species (ROS) which irreversibly damage cancer cells.[12–14] Nanomedicine containing ScNPs such as nanoparticles with high Z-elements or metal nanoclusters have been observed to be an effective methodology to enhance PDT efficacy under X-ray irradiation.[15,16] In this paradigm, ScNPs combined with porphyrin or organic dye as photosensitizers are glaringly investigated *in vitro* and *in vivo* to kill cancer cells or to destroy solid tumors.[17,18] Amusingly, low dose treatment is the major advantage of X-RDT, but it still faces a lack of radiosensitivity. In order to accomplish splendid therapeutic efficacy, Lin and co-workers have successfully designed a hafnium (Hf)–Ru based nanoscale metal organic framework (nMOF) for mitochondria targeted X-ray induced radiation and radiodynamic therapy (X-RT-RDT) under low dose X-ray irradiation.[19] In the Hf–Ru based nMOF, Hf could act as an X-ray scintillator, and transfer high energy X-rays into light for the Ru-complex photosensitizer to produce singlet oxygen ($^1O_2$). Additionally, Hf as an X-ray radiosensitizer was capable of generating hydroxyl radicals from adjacent water molecules resulting in enhancement of RT efficacy. However, high quantum yield and long life time of the photosensitizers are the imperative properties for superior RDT efficacy.[20] Recently, the Chen group has well designed a metal doped silicate nanosensitizer conjugated with an effective photosensitizer, rose Bengal (RB) as a new X-PDT agent which exhibited significant inhibitory effect on tumor progression under low dose X-ray irradiation.[21] In order to improve X-RT, radiosensitizers (RS) have been immensely used for X-ray irradiated auger therapy (AT) in which low energy auger electrons disrupt directly DNA strands.[22–24] The main attracting advantage of X-ray irradiated auger therapy (AT) is the continues generation of auger electrons upon single dose X-ray irradiation, which is unlike the frequent use of X-rays in conventional RT.[25]

Hence, to address the effective efficacy for both X-RT by auger electrons and X-RDT by producing $^1O_2$, X-ray inducible radiation and radiodynamic therapy (X-RRDT) could build a revolution in the entire discipline of cancer treatment. Several recent studies have reported the significant radiosensitizing and scintillating properties of octahedral molybdenum clusters under X-ray irradiation.[26,27] Herein, we established the largest strawberry shaped polyoxomolybdate nanoclusters (POMo NCs) which exhibited radiosensitizing features by producing auger electrons and scintillating properties upon X-ray irradiation. To date, investigations on POMo NCs as an X-RT agent and POMo NCs-photosensitizer based X-RDT agents for tumor destruction have not yet been studied. Meanwhile, rose Bengal (RB) as a photosensitizer is massively used in light induced PDT due to the generation of abundant $^1O_2$ with high quantum yield.[28–30] Therefore, the design of nanoformulations composed of POMo NCs as an X-ray radiosensitizer and X-ray scintillator with RB as a photosensitizer could be an advanced technique for X-RRDT to combat cancer.

In this work, we successfully synthesized POMo NCs and RB loaded PEG functionalized chitosan (CS) nanoformulations (PEGylated POM@CS–RB) as X-ray radiosensitizors and X-ray scintillators. Hollow structured CS for RB loading in their cavity to a large extent and simultaneously their cationic surface charge assisted to hold anionic POMo NCs firmly. Importantly, the remarkable radiosensitizing properties of the POMo NCs expedited X-ray induced RT as strongly evidenced by γ-H_2AX assay. Moreover, X-ray inducible excellent RDT efficacy by POMo NCs arose from their incredible scintillating properties in which the transduced energy stimulated RB to generate cytotoxic $^1O_2$ as confirmed from the SOSG assay kit study extra and intracellularly. However, the mutual consequence of RT and RDT from POMo@CS–RB leading to the damage of DNA which in turn resulted in killing of cancer cells was successfully evidenced by both γ-H_2AX and live/dead cell co-staining assay. For instance, robust NIR absorbance of POMo NCs at 860 nm resulted in photoacoustic imaging (PA) guided X-ray inducible radiation and radiodynamic therapy (X-RRDT) *in vivo*. Finally, *in vivo* study revealed the effective outcome in regression of the tumor growth without triggering side effects in major normal organs as demonstrated by hematoxylin and eosin (H&E) staining. However, the continuous production of auger electrons from POMo NCs under single dose X-ray irradiation could be advantageous for low dose treatment. Additionally, the low dose treatment might protect the other normal organs from serious damage. Hence, our projected nanomaterials, PEGylated POMo@CS–RB could be successfully applied for clinical trials as X-RRDT agents for cancer treatment in the future.

Results and discussion

The detailed synthesis procedure for the formation of POMo nanoparticles (NPs), POMo NCs and hollow chitosan as well as the designing of PEGylated POMo@CS–RB have been discussed in the methods section. In brief, POMo nanoclusters (NCs) were obtained by reduction of phosphomolybdic acid in a mild alkaline medium followed by cryodesiccation. POMo NCs were added to freshly prepared CS solution and then stirred for 24 h under dark conditions. After removal of unloaded POMo, the yellowish blue solution was collected, yielding POMo loaded CS (POMo@CS) nano-formulation. Next, POMo@CS–RB was prepared by adding RB solution in POMo@CS solution. Polyethylene glycol (PEG) was used to modify the POMo@CS–RB nanoformulation to make it biocompatible. The overall design of PEGylated POMo@CS–RB and the plausible mechanism of auspicious mutual radiosensitization with scintillating properties for X-RRDT have been schematically demonstrated in Fig. 1. In short, upon X-ray irradiation, POMo NCs could constantly generate auger electrons to break DNA, improving RT efficacy. Meanwhile, POMo NCs could also transfer high energy X-rays into visible light to stimulate RB for production of $^1O_2$ which damaged DNA indirectly.

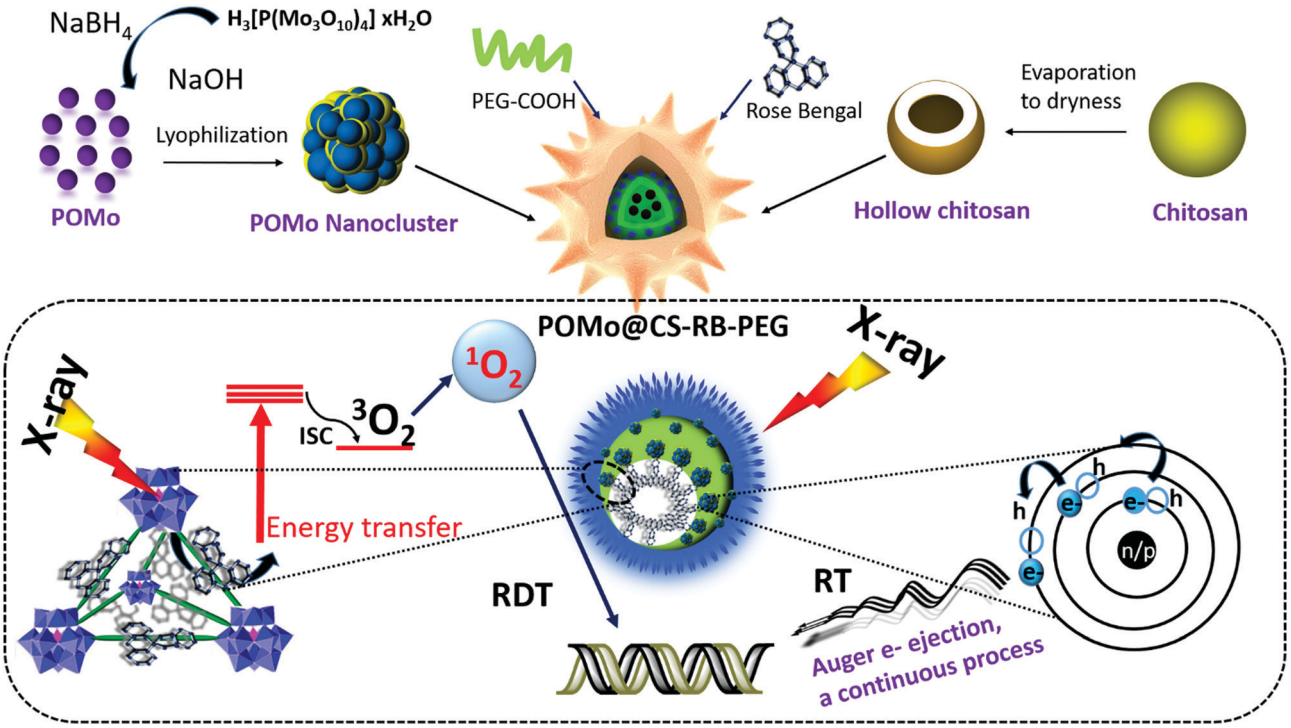

Fig. 1 The schematic presentation for designing PEGylated POMo@CS–RB nanoformulations and the plausible mechanism of X-ray inducible RRDT. Upon X-ray irradiation, electrons from a higher energy orbital falls into a lower energy orbital to fill the vacancy by releasing energy as an auger electron of the Mo atom in the POMo nanocluster. The auger electron causes DNA damage directly. Under X-ray irradiation, POMo NCs exhibited scintillating properties by transferring high energy into light which stimulated RB to create its most stable excited triplet state. At the triplet state, RB could generate $^1O_2$ with high quantum yield from molecular oxygen. The as produced $^1O_2$ caused DNA damage indirectly.

X-ray diffraction (XRD) patterns of POMo NCs were matched well with the previously reported articles[31] (ESI,† Fig. S1). An interesting investigation on structural analysis by macromodel-2 (MM-2) study revealed that strawberry shaped POMo NCs composed of 652 Mo atoms with overall size of 5.9 nm were structurally formed which was nicely corroborated by transmission electron microscope (TEM) images. To the best of our knowledge, this was the largest POMo cluster containing 163 Mo (Mo)3 units of three edge sharing MoO_6 octahedra and connecting to the central PO_4 octahedron (Fig. 2a). This structure was formed following the kegging structure of $PMo_{12}O_{40}$.[32] As shown in Fig. 2b and c, the crucially optimized strawberry structured POMo NC is shown by both stick-ball and space fill style, respectively. On controlled reduction of Mo(VI) to Mo(V), both oxidation states (VI/V) of Mo in POMo NCs persisted as determined by X-ray photoelectron spectroscopic (XPS) analysis (Fig. 2d). The full XPS spectrum of POMo NCs is presented in the ESI,† Fig. S2. Additionally, the intense peak at 670 nm was attributed to the metal to metal charge transfer between Mo(VI) and Mo(V), further assuring their simultaneous presence in the cluster (ESI,† Fig. S3). However, the sharp peak at 862 nm was ascribed to the charge transfer from oxygen to Mo(V), resulting in blue color. The monodispersed POMo NCs with an average size of 6 nm (histogram inset) were uniformly distributed on CS as shown by TEM images (Fig. 2e and f). Moreover, a uniform hollow structure in the CS was clearly observed by TEM images. The surface modified POMo loaded CS (PEGylated POMo@CS) exhibited an average size of 80 nm (histogram inset, Fig. 2b), whereas, dynamic light scattering (DLS) measurement showed a *Z*-average of 106 nm with polydispersity index of 0.134 ± 0.02 (ESI,† Fig. S4). Good distributions of molybdenum (Mo) and oxygen were successfully analyzed by TEM elemental mapping (Fig. 2c). The high Brauner Emmett Teller (BET) surface area and the Barret Joyner Halenda (BJH) pore size of PEGylated POMo@CS were measured to be ~97 m^2 g^{-1} and ~50 nm, respectively, further ensuring the formation of hollow structured CS (ESI,† Fig. S5).

As expected, during RB loading, a large amount of RB was effectively loaded into the cavity of hollow CS. The successful loading of various concentrations of RB was examined from the characteristic UV-visible-NIR absorbance of RB at 530 nm (ESI,† Fig. S6a). The loading efficiency (POMo@CS:RB, w/w) was enhanced with increasing the concentration of RB and the utmost RB loading efficiency was calculated to be 68% (ESI,† Fig. S6b). The loaded RB in the POMo@CS–RB nanoformulation was very stable in different solutions including deionized water and phosphate buffer solution (PBS). Only less than 10% of RB could be released from the POMo@CS–RB nanoformulation (ESI,† Fig. S6c). Additionally, we also tested the stability of the POMo@CS–RB nanoformualtion in different pH (pH 7.4 and 6.5) solutions. It was found that the size of the POMo@CS–RB nanoformulation exhibited no obvious change in different pH solutions, indicating good stability of the nanoformualtion (ESI,† Fig. S7). Such a high amount of RB

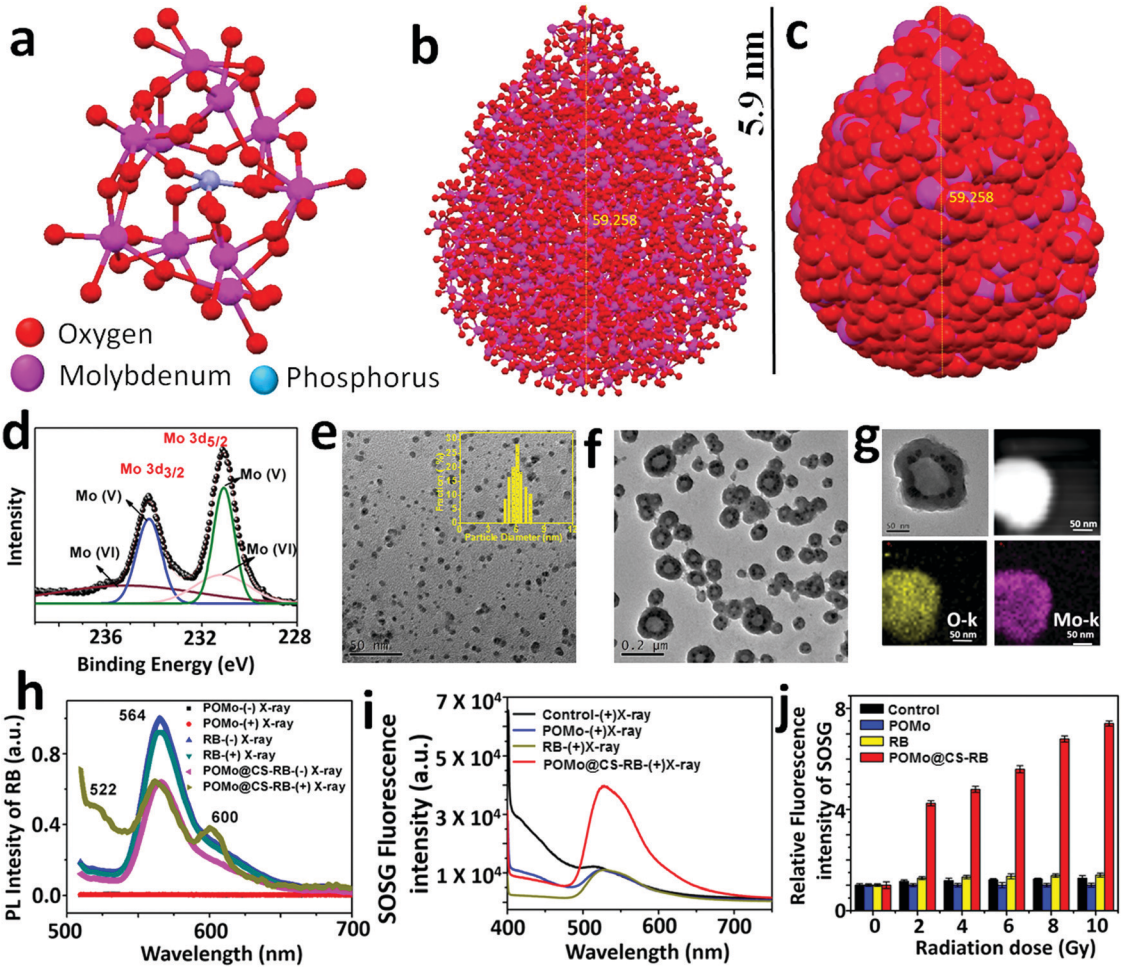

Fig. 2 Characterization of POMo NCs and X-ray response behaviour of POMo NCs containing different nanomaterials. (a) Kegging structure of Mo_5O_{21} in which each Mo atom shares three O atoms to other three Mo atoms and two O atoms are free. Strawberry shaped POMo NCs were obtained by connecting octahedral MoO6 units in kegging structure type: (b) ball and stick style and (c) space fill style. The strawberry shape was optimized after obtaining the same structure repeated five times. (d) XPS spectra of POM NCs. (e) TEM image of POMo NCs (histogram inset). (f) TEM image of PEGylated POMo@CS. (g) Elemental mapping of PEGylated POMo@CS. (h) Photoluminescence (PL) spectra of POM@CS–RB, irradiated and non-radiated by X-rays (2 Gy). (i) Fluorescence spectra of SOSG in the solution of different nanomaterials under X-ray irradiation (2 Gy). (j) Relative fluorescence intensity of SOSG in the solution of different nanomaterials under different X-ray doses.

loading was due to the incorporation of dye molecules inside the cavity of hollow CS. However, the fine and firm orientation of the POMo NCs onto the CS was well explained from surface charge analysis as measured by zeta potential (ESI,† Fig. S8). The zeta potential of chitosan nanoparticles and POMo NCs was measured to be +31 and −9 mV, respectively. Therefore, the adequate distribution of anionic charged POMo NCs onto cationic CS was possible due to the effective ionic interaction between them. Nevertheless, after RB loading, the positive surface charge of POMo@CS was decreased by 2 mV, further confirming RB loading in the cavity of hollow CS. Furthermore, the positive surface charge of +18 mV for POMo@CS was abruptly reduced to +6 mV after PEG modification. Almost neutral surface charge of PEGylated POMo@CS would enhance its mobility through the blood stream during the animal experiment.

In order to evaluate the scintillating characteristics of POMo NCs upon X-ray irradiation, a photoluminescence (PL) study was assertively conducted (Fig. 2h). Bare POMo NCs exhibited no optical features. However, the RB showed a single strong broad emission centred at 566 nm upon excitation at 490 nm before and after X-ray treatment. A similar result was observed for RB loaded POMo@CS before X-ray irradiation. Interestingly, miniature observation revealed that two more peaks at 522 and 602 nm for RB loaded POMo@CS nanoparticles were intensified after X-ray treatment, while the most common peak of RB was at 566 nm at the same excitation energy. Here, we called these two peaks as phantom peaks because these appeared only for X-ray treated RB loaded POMo@CS. The appearance of the two phantom peaks could be explained as the occurrence of several redox reactions among the various reduced and oxidized states of RB which were produced at the excited triplet state of RB.[33] It assumed that POMo NCs could act as an energy transducer. Upon X-ray irradiation, POMo NCs could transfer incident high energy into visible light which could stimulate the RB in

sequence to create its excited state. Since, RB is a prominent photosensitizer to generate colossal $^1O_2$ from molecular oxygen at its triplet excited state, it could be possible for plentiful generation of $^1O_2$ upon falling X-rays on RB loaded POMo NCs.

The feasibility for the generation of singlet oxygen by POMo, RB or POMo@CS–RB was assessed by a single oxygen sensor green (SOSG) indicator. By measuring the fluorescence signal of SOSG, $^1O_2$ is easily be detected in both extra and intracellular circumstances.[34] However, in our experiment, 100 μM of SOSG was added to deionized water or aqueous solution of RB or water dispersed POMo or POMo@CS–RB at an RB and Mo concentration of 50 and 100 μg mL^{-1}, respectively, and then irradiated with X-rays at 2 Gy. As shown in Fig. 2i, strong fluorescence intensity of SOSG for POMo@CS–RB treated solution was detected, while almost no response from other nanomaterials was observed. It could only be possible if POMo nanoclusters exhibited scintillating features under high energy electromagnetic radiation. Hence it was anticipated that upon X-ray irradiation, POMo nanoclusters might transfer the high energy into visible light which in turn activated RB to produce $^1O_2$. Meanwhile, the same experiment was conducted at different X-ray doses in the range between 0 and 10 Gy and the production of singlet oxygen was quantified by measuring the fluorescence intensity of SOSG. With increasing X-ray doses, the fluorescence intensity of SOSG was sharply amplified for POMo@CS–RB, while negligible intensity was perceived for the rest of the tested samples (Fig. 2j). Furthermore, in order to determine whether hydroxyl radicals (•OH) as ROS were generated upon X-ray irradiation at a low dose, we carried out the *p*-aminophenyl fluorescein (APF) assay. APF could react with •OH resulting in a strong fluorescence at 515 nm at an excitation wavelength of 490 nm.[35,36] No prominent peak (data not shown) suggested that the excited triplet state of RB was proceeded importantly *via* the type II pathway.

In aid of therapeutic performance of the synthesized X-RRDT nanoformulation, it is necessary to check its activity towards cells and ability to localize to the site of the disease. Therefore, to image the intracellular distribution of the PEGylated POMo@CS–RB nanoformulation, we performed fluorescence imaging on 4T1 cells by using confocal laser scanning microscopy (CLSM) after incubation of the nanomaterial for 12 h at 37 °C. The cell nucleus was stained with 4′,6-diamidino-2-pheylindole (DAPI) (blue) and the green fluorescence of the fluorescein isothiocyanate (FITC) conjugated POMo@CS–RB nanoformulation was observed in all the cells. The strong green fluorescence was spotted around the cell nucleus and preferentially distributed across the cytoplasm (Fig. 3a). The good internalization of the nanomaterials by the cells depended on endocytosis.

Henceforth, *in vitro* toxicity of the bare RB, PEGylated POMo@CS and POMo@CS–RB nanoformulations towards 4T1 cells with and without X-ray irradiation was studied by 3-(4,5-dimethylthiazol-2-yl)-2,5diphenyltetrazolium bromide (MTT) assay. The control nanoparticles without X-ray treatment caused no toxicity to cells. The cells were viable virtually up to 95% at high concentration of both POMo (500 μg mL^{-1}) and RB (200 μg mL^{-1}) (ESI,† Fig. S9). Therefore, the results of the cell viability suggested that all nanoformulations were biocompatible to the 4T1 cells. In disparity, upon 2 Gy of X-ray irradiation, the PEGylated POMo@CS nanoparticles caused a minute toxicity to the cells at low concentration of POMo NCs and cell viability was gradually dropped with increasing the concentration of POMo (Fig. 3d). This result specified that POMo NCs could perform as a fabulous X-ray radiosensitizer *via* X-ray inducible RT. However, RB induced no toxicity to the cell upon X-ray treatment. Importantly, at very low concentration of both POMo and RB, the PEGylated POMo@CS–RB nanoformulation manifested a substantial death of 4T1 cells under very low dose of X-ray irradiation (2 Gy) *via* X-ray inducible radiation and radiodynamic therapy (X-RRDT).

The hollow structure of CS could provide a novel nanoplatform to load RB with a high content. In aid of the massive generation of extracellular $^1O_2$, we hypothesized that POMo NCs might relay energy in the form of visible light to stimulate RB to produce $^1O_2$ upon X-ray irradiation. To validate the effect in detection of the ample generation of intracellular $^1O_2$, singlet oxygen sensor green (SOSG) was used to detect $^1O_2$. The cells incubated with PEGylated POMo@CS–RB nanoparticles and irradiated by X-rays exhibited strong green fluorescence signal. While minimal fluorescence signals were visualized for the other X-ray treated nanomaterials such as PBS, RB or PEGylated POMo@CS (Fig. 3b). Meanwhile, the fluorescence intensity of SOSG was detected by flow cytometry analysis. For X-ray treated PEGylated POMo@CS–RB nanoparticles, obtaining superior fluorescence intensity with diminished cell count confirmed that colossally generated $^1O_2$ caused death of the cells probably *via* X-ray inducible radiodynamic therapy (X-RDT) (Fig. 3c). However, for X-ray treated RB or PEGylated POMo@CS, no specious change was perceived in both the fluorescence intensities of SOSG and in cell count from X-ray irradiated PBS. Therefore, from *in vitro* data (Fig. 3d), we could speculate indirectly that the POMo@CS–RB nanoformualtion could transfer the high energy into visible light which in turn stimulated the RB to produce $^1O_2$ for killing cancer cells.

Encouraged by the radiosensitization effect of POMo NCs, we performed a DNA strands break immunofluorescence staining assay using phosphorylated γ-H_2AX, a sensitive protein biomarker to detect DNA damage induced by ionizing radiation. Upon X-ray irradiation at a dose of 2 Gy, red fluorescence of γ-H_2AX was alleged for both POMo and RB loaded POMo NCs, indicating the breakages of DNA double strands in the nuclei of the cells (Fig. 4a). POMo@CS–RB under X-ray irradiation would generate abundant ROS and decrease DNA damage repair ability in the cytoplasm. Therefore, the POMo@CS–RB nanoformulation could significantly induce DNA damage. The results further confirmed that POMo nanoclusters could act as X-ray radiosensitizers which triggered DNA damage *via* X-ray inducible radiation therapy (X-RT). Furthermore, strong red fluorescence was more intensified from the nuclei for POMo@CS–RB treated cells. In addition, no indication of fluorescence signal in PBS or RB treated cells at the same X-ray irradiation dose reversely supported the radiosensitization effect of POMo nanoclusters (Fig. 4a).

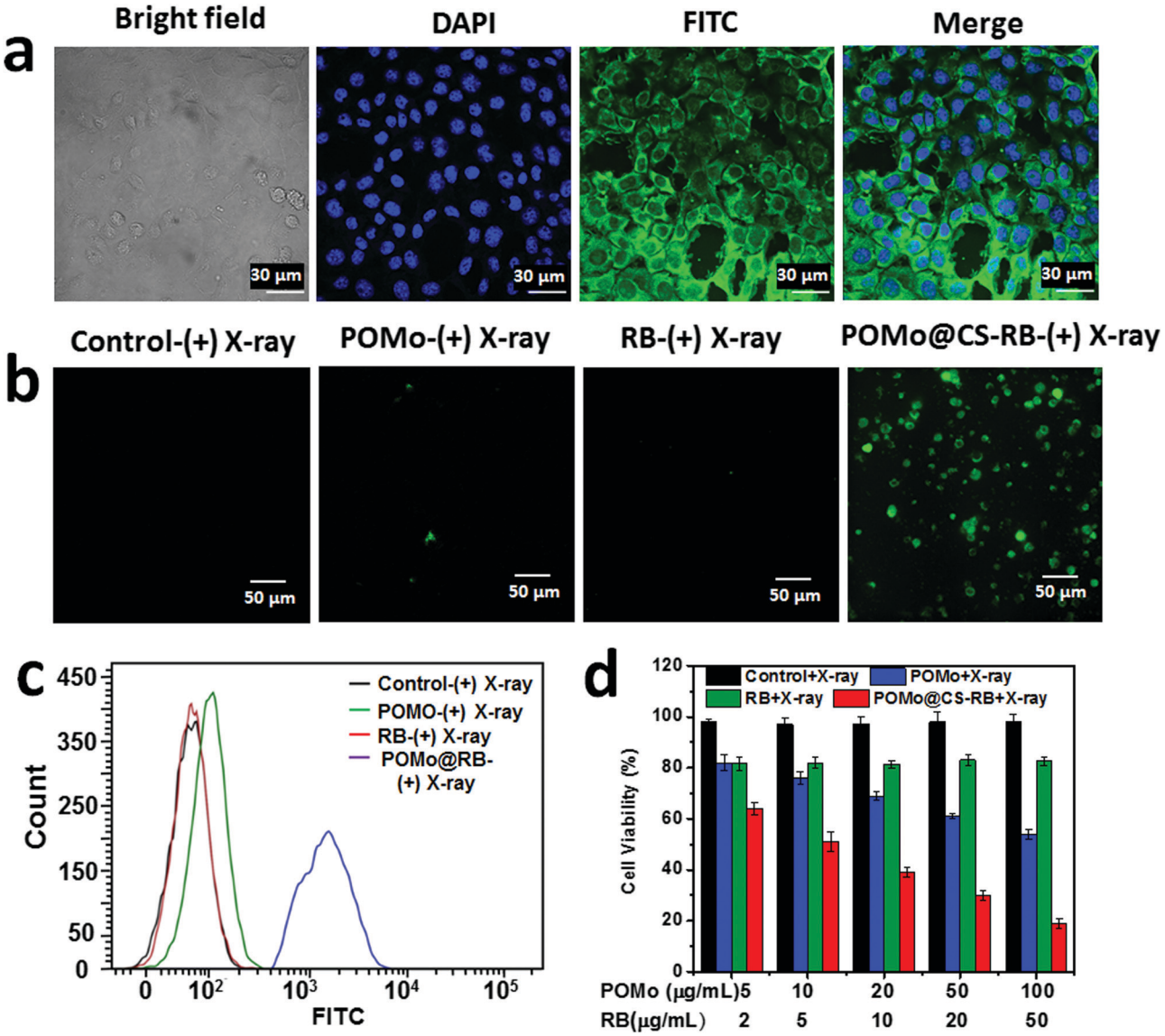

Fig. 3 *In vitro* study on 4T1 cells. Confocal imaging for (a) cellular uptake by showing bright field, nuclei stained with DAPI (blue), green fluorescence of FITC and merge after 24 h incubation at 25 °C. (b) Confocal imaging for singlet oxygen generation using an SOSG assay and (c) flow cytometry measurement of cellular SOSG fluorescence for cells treated with PBS + X-ray, POMo + X-ray, RB + X-ray, and POMo@CS–RB + X-ray, respectively. (d) Cell viability data obtained from MTT assay of 4T1 cells after various treatments indicated. Relative cell viabilities in all the samples were normalized to the control saline-added without X-ray irradiation (100% viability). Error bars were based on standard deviation.

In order to confirm the feasibility of X-ray inducible radiation and radiodynamic therapy (X-RRDT) synergistically influenced by radiosensitization and the scintillation effect of PEGylated POMo@CS–RB to kill cancer cells, calcine-AM and propidium iodide (PI) co-staining assays were performed on 4T1 cells to detect live and dead cells after different treatments. For RB treated cells, only green fluorescence signals analogous to the live cells were visualized upon X-ray irradiation similar to the PBS treated cells (Fig. 4b). These observations were well matched with cell viability results, further ensuring that RB merely was unable to combat against cancer cells even after X-ray irradiation. Meanwhile, numerous strong green signals were observed in PEGylated POMo@CS treated cells, demonstrating the X-ray radiosensitization effect of POMo nanoclusters (Fig. 4b). Thus, under X-ray treatment, PEGylated POMo@CS assisted to kill the cancer cells to a little extent *via* X-RT. However, X-ray inducible communal outcome from radiosensitization and the scintillation effect made the PEGylated POMo@CS–RB nanoformulation an effective X-RRDT agent to fight against cancer cells by completely killing them.

The photoacoustic (PA) imaging technique is abruptly used to capture images of the foreign nanomaterials in the different organs. The hasty accumulation and long-time retention of the nanoformulations in the tumor site was evidenced by time dependent PA imaging as shown in Fig. 4c. Since POMo with strong NIR absorbance could act as an excellent PA contrast agent,[37] the strong PA signal at 2 h post injection assured the rapid accumulation of the nanoformulations in the

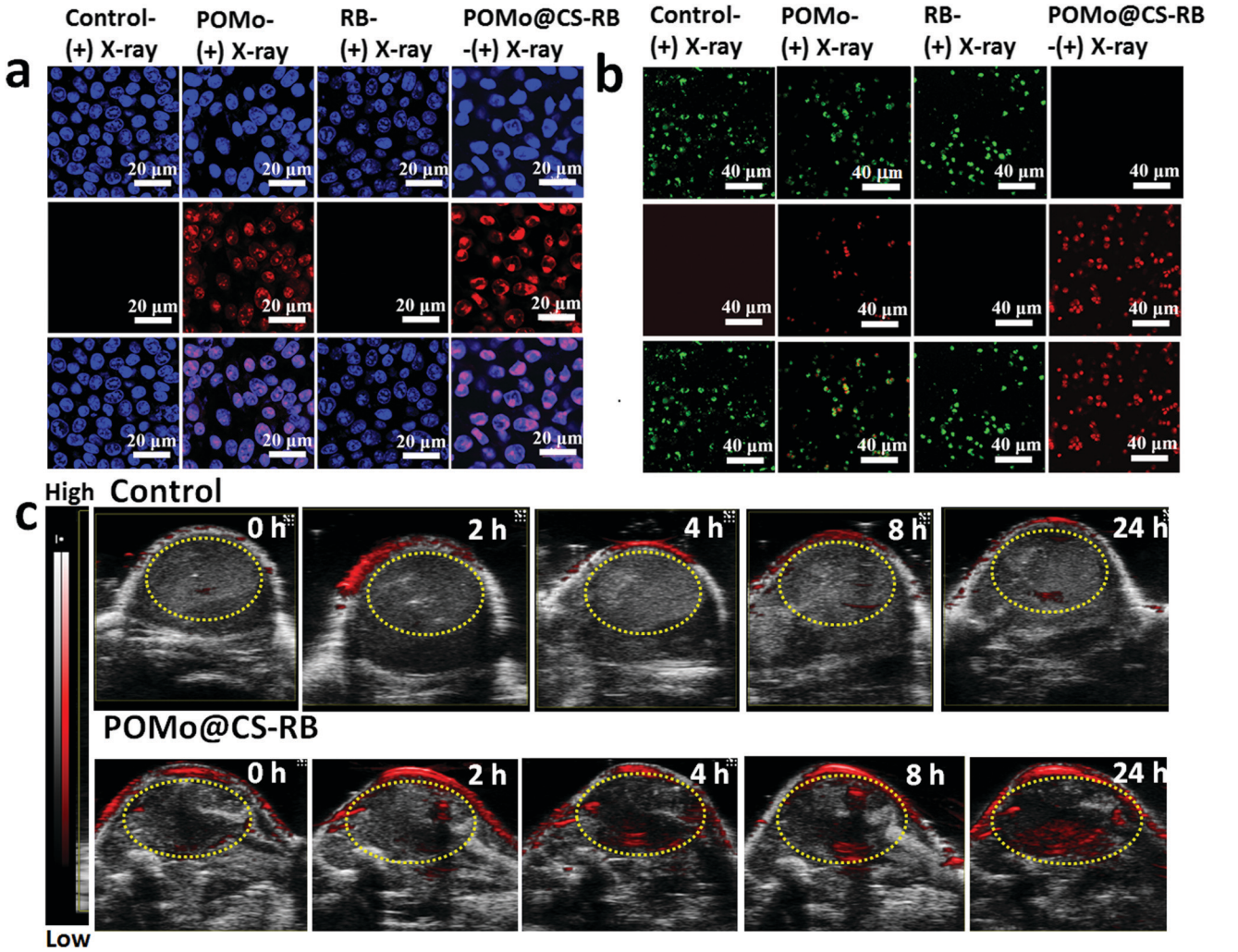

Fig. 4 *In vitro* X-RRDT on 4T1 cells and *in vivo* PA imaging on 4T1 tumor bearing mice. (a) Immunofluorescence staining assay using phosphorylated γ-H_2AX for DNA damage study after different treatments. (b) Calcein-AM/PI co-staining assay for live/dead cell detection after different treatments. The treatments were conducted using PBS + X-ray, POMo + X-ray, RB + X-ray, and POMo@CS–RB + X-ray, respectively. (c) PA imaging at different time points after intravenous injection of PBS or PEGylated POMo@CS–RB.

tumor site (ESI,† Fig. S3). The signal strength was intensified over time, suggesting the retention of the nanoformulation in the tumor region.

The quantitative measurement of the Mo levels in the mouse body was conducted by the *ex vivo* inductively coupled plasma atomic emission spectroscopy (ICP-AES) technique. The blood circulation of PEGylated POMo@CS–RB was studied after intravenous injection into the 4T1 tumor bearing mice. The collected blood samples were studied to measure the concentration of Mo in the blood by ICP-AES. The amount of POMo@CS–RB in the blood was decreased with increase in time according to a two-compartment model (Fig. 5a). The first ($t_{1/2}(\alpha)$) and second ($t_{1/2}(\beta)$) phases of circulation half-lives were calculated to be 5.09 ± 0.4 h and 9.9 ± 0.3 h, respectively. According to the literature reports,[38–40] PEG modification could significantly prolong the blood circulation of nanomaterials. Therefore, such long-time blood circulation of the POMo@CS–RB nanoformulation could avoid it being quickly swallowed by the reticuloendothelial system (RES). The half-lives of the POMo@CS–RB nanoformulation in the mice exhibited long-time circulation. To assess the effectiveness of POMo@CS–RB delivery, its biodistribution in normal organs and 4T1 xenograft tumors was examined by quantifying Mo content (Fig. 5b). As expected, POMo@CS–RB exhibited rapid accumulation and long term retention in the tumor lesion after intravenous injection. The tumor uptake value was measured to be 11.2 ± 2.1 and 15.3 ± 3.2 ID g^{-1} at 1 and 24 h, respectively.

Considering persistent ejection of auger electrons from POMo NCs and constant generation of $^1O_2$ from POMo@CS–RB concurrently with long term retention of PEGylated POMo@CS–RB inside the tumor, *in vivo* X-ray inducible RRDT was performed. Mice bearing 4T1 tumors with initial volumes of 100 mm^3 were chosen and subjectively divided into five groups with five mice in each group. Each group of mice was intravenously injected with PBS, POMo, RB and POMo@CS–RB (two groups). All the treated mice were subjected to irradiation by X-rays at 2 Gy except for one group treated by POMo@CS–RB.

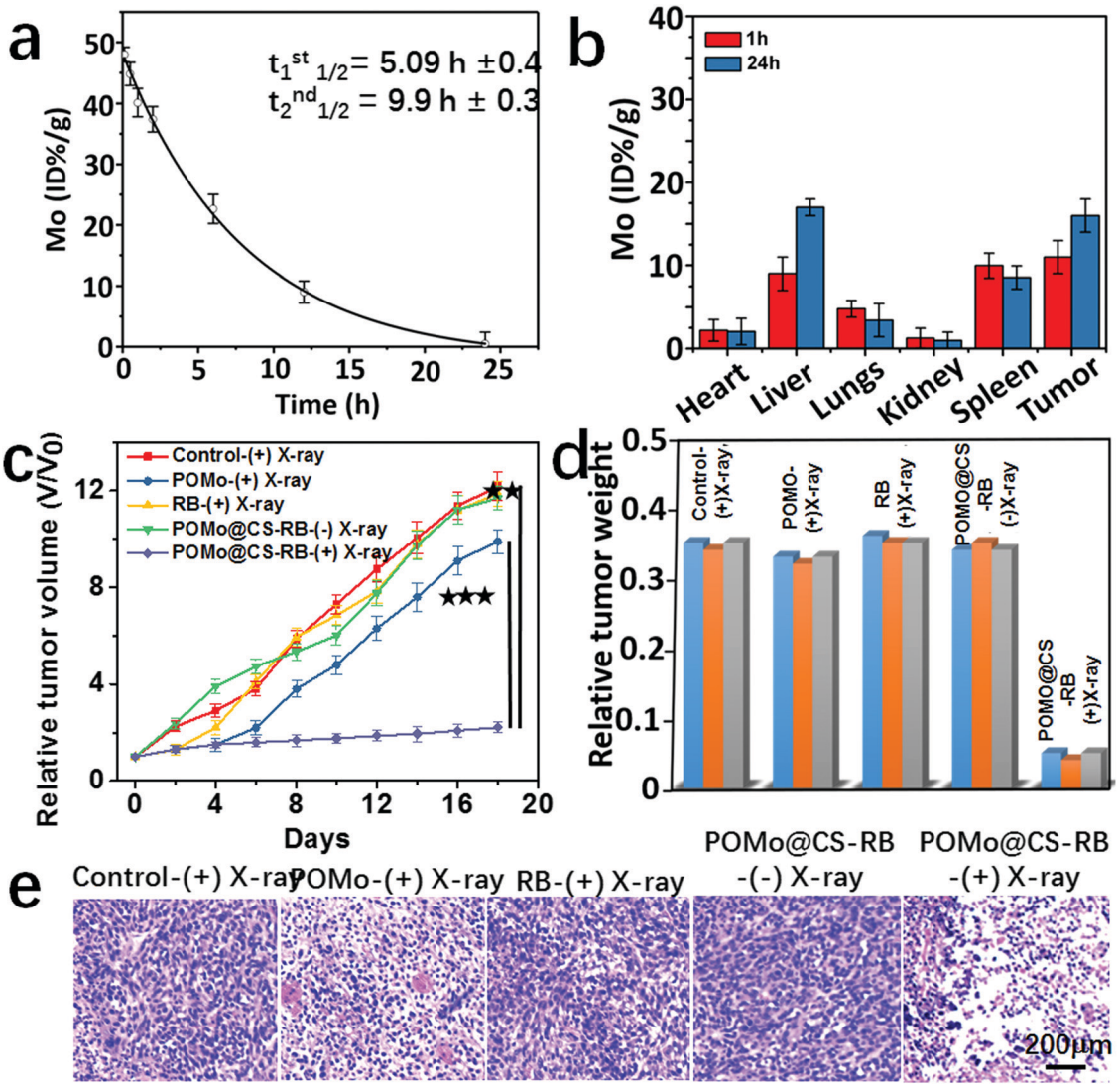

Fig. 5 *In vivo* X-RRDT. (a) Plasma concentration of Mo from the mice treated with PEGylated POMo@CS–RB at a dose of 25 mg of Mo kg^{-1} at different time points. (b) Bio-distribution of Mo in various major tissues of the mice treated with PEGylated POMo@CS–RB at a dose of 25 mg of Mo kg^{-1} collected at two different time points. (c) Relative tumor volume patterns of different groups of mice after the various treatments indicated (**$p < 0.01$, ***$p < 0.001$). (d) Relative tumor weight of different groups of mice after various treatments. (e) H&E stained tumor slices from different groups of mice treated with PBS + X-ray, POMo + X-ray, RB + X-ray, POMo@CS–RB – X-ray and POMo-RB + X-ray, respectively. The tumors were harvested 2 days after treatments were conducted. Error bars are based on standard errors of the mean.

After careful treatment, the length and width of the tumors were checked using a digital caliper at two day intervals for the next 18 days as shown in Fig. 5c. The tumors treated with PBS expanded day by day piercingly, and within 18 days the tumors volume attained the maximum value. An almost similar rate of tumor growth was observed for the group of mice treated with RB under X-ray irradiation, strictly due to the no radiosensitivity of RB under X-rays. Fascinatingly, mice treated with PEGylated POM@CS exhibited reduced tumor growth rate, owing to the rigorous radiosensitivity of POMo NCs under X-ray treatment. However, unfortunately, after one week, a steady increase in tumor volume was perceived. Remarkably, the tumor growth in the group of mice treated with POMo@CS–RB was significantly inhibited, likely owing to the mutual effect of radiosensitization and scintillation from POM@CS–RB under X-ray irradiation. Such excellent therapeutic efficiency further demonstrated the successful radiation and radiodynamic therapy for cancer treatment. Meanwhile, no changes in the body weights of the mice were noticed after various treatments, suggesting no palpable side effect in our animal experiment as shown in the ESI,† Fig. S10. The tumors weight for the POMo@CS–RB treated group were significantly low relative to that of other treated groups (Fig. 5d). Furthermore, the noticeable anti-tumor efficacy of the POMo@CS–RB was well confirmed by H&E evaluation (Fig. 5e). The tumors treated with RB after X-ray treatment and the tumors treated with PEGylated POMo@CS in the absence of X-rays manifested closely arranged cancer cells as similar to the tumors in the saline control group.

Whereas, the tumors of mice treated with POMo displayed cell shrinkage and intercellular blank. Moreover, the tumor tissues flensed from the mice injected with POMo@CS–RB comprised very few cancer cells and had the highest level of tumor necrosis. These results were in good agreement with those of the tumor growth inhibition study. No perceptible changes in the different tissues of the major organs, including the kidneys, liver, and spleen from the control group treated organs were noticed, demonstrating the good biocompatibility of the POMo@CS–RB nanoformulation (ESI,† Fig. S11). The results strongly supported that our designed PEGylated POMo@CS–RB nanoformulation could perform as an effective X-RRDT agent under very low dose X-ray radiation without damaging other organs.

Conclusions

In summary, to date for the first time, we have synthesized the largest strawberry shaped POMo NCs which exhibited both X-ray radiosensitizing and X-ray scintillating properties. POMo NCs and RB were successfully designed as an effective X-RRDT agent for cancer therapy. Upon single dose X-ray treatment, constant generation of auger electrons from POMo NCs led to enhanced X-RT efficacy. However, continuous generation of auger electrons and ample production of $^1O_2$ from POMo@CS–RB under X-ray radiation resulted in X-ray inducible RRDT for cancer treatment. Meanwhile, high tumor accumulation and longtime retention of the PEGylated POMo@CS–RB nanoformulations in the tumor site significantly inhibited the tumor growth under X-ray irradiation at a low dose. Therefore, our developed strategy will further promote the cancer therapeutic efficiency under low dose X-ray radiation, and bring hope for clinical cancer treatment.

Conflicts of interest

There are no conflicts to declare.

Acknowledgements

This work was partially supported by the National Natural Science Foundation of China (31822022), a Jiangsu Natural Science Fund for Outstanding Youth Science Foundation (BK20180094), and a Project Funded by the Priority Academic Program Development of Jiangsu Higher Education Institutions (PAPD).

Notes and references

1 J. Thariat, J. M. Hannoun-Levi, A. Sun Myint, T. Vuong and J. P. Gerard, *Nat. Rev. Clin. Oncol.*, 2013, **10**, 52–60.
2 D. Schaue and W. H. McBride, *Nat. Rev. Clin. Oncol.*, 2015, **12**, 527–540.
3 A. Bansal, F. Yang, T. Xi, Y. Zhang and J. S. Ho, *Proc. Natl. Acad. Sci. U. S. A.*, 2018, **115**, 1469–1474.
4 I. Mfouo Tynga and H. Abrahamse, *Nanomaterials*, 2018, **8**, 923.
5 L. Cheng, C. Wang, L. Z. Feng, K. Yang and Z. Liu, *Chem. Rev.*, 2014, **114**, 10869–10939.
6 M. I. Khot, H. Andrew, H. S. Svavarsdottir, G. Armstrong, A. J. Quyn and D. G. Jayne, *Clin. Colorectal Cancer*, 2019, **18**(2), e200–e209.
7 I. Niagara Muhammad, G. Muthu Kumara, Z. Jing, P. C. Ho, M. Ratha and Z. Yong, *Nat. Med.*, 2012, **18**, 1580.
8 D. Kwatra, A. Venugopal and S. Anant, *Transl. Cancer Res.*, 2013, **2**, 330–342.
9 G. Lan, K. Ni, R. Xu, K. Lu, Z. Lin, C. Chan and W. Lin, *Angew. Chem., Int. Ed.*, 2017, **56**, 12102–12106.
10 X. D. Ren, X. Y. Hao, H. C. Li, M. R. Ke, B. Y. Zheng and J. D. Huang, *Drug Discovery Today*, 2018, **23**, 1791–1800.
11 B. Cline, I. Delahunty and J. Xie, *Wiley Interdiscip. Rev.: Nanomed. Nanobiotechnol.*, 2019, **11**, e1541.
12 A. Karnkaew, F. Chen, Y. H. Zhan, R. L. Majewski and W. B. Cai, *ACS Nano*, 2016, **10**, 3918–3935.
13 H. Chen, G. D. Wang, Y. J. Chuang, Z. Zhen, X. Chen, P. Biddinger, Z. Hao, F. Liu, B. Shen, Z. Pan and J. Xie, *Nano Lett.*, 2015, **15**, 2249–2256.
14 H. Wang, B. Lv, Z. Tang, M. Zhang, W. Ge, Y. Liu, X. He, K. Zhao, X. Zheng, M. He and W. Bu, *Nano Lett.*, 2018, **18**, 5768–5774.
15 C. C. Hsu, S. L. Lin and C. A. Chang, *ACS Appl. Mater. Interfaces*, 2018, **10**, 7859–7870.
16 L. S. Tew, M. T. Cai, L. W. Lo, Y. L. Khung and N. T. Chen, *Materials*, 2018, **11**, 1170.
17 S. Clement, W. Deng, E. Camilleri, B. C. Wilson and E. M. Goldys, *Sci. Rep.*, 2016, **6**, 19954.
18 R. Tatti, M. Timpel, M. V. Nardi, F. Fabbri, F. Rossi, L. Pasquardini, A. Chiasera, L. Aversa, K. Koshmak, A. Giglia, L. Pasquali, T. Rimoldi, L. Cristofolini, G. Attolini, S. Varas, S. Iannotta, R. Verucchi and G. Salviati, *Mol. Syst. Des. Eng.*, 2017, **2**, 336.
19 K. Ni, G. Lan, S. S. Veroneau, X. Duan, Y. Song and W. Lin, *Nat. Commun.*, 2018, **9**, 4321.
20 Z. S. Al-Ahmady, C. L. Scudamore and K. Kostarelos, *Int. J. Cancer*, 2015, **137**, 731–743.
21 W. Sun, T. Shi, L. Luo, X. Chen, P. Lv, Y. Lv, Y. Zhuang, J. Zhu, G. Liu, X. Chen and H. Chen, *Adv. Mater.*, 2019, 1808024.
22 B. Cornelissen and K. A. Vallis, *Curr. Drug Discovery Technol.*, 2010, **7**, 263–279.
23 H. Thisgaard, B. Halle, C. Aaberg-Jessen, B. B. Olsen, A. S. N. Therkelsen, J. H. Dam, N. Langkjaer, S. Munthe, K. Nagren, P. F. Hoilund-Carlsen and B. W. Kristensen, *Theranostics*, 2016, **6**, 2278–2291.
24 F. Buchegger, F. Perillo-Adamer, Y. M. Dupertuis and A. B. Delaloye, *Eur. J. Nucl. Med. Mol. Imaging*, 2006, **33**, 1352–1363.
25 R. W. Howell, *Int. J. Radiat. Biol.*, 2013, **89**, 593.
26 D. V. Evtushok, A. R. Melnikov, N. A. Vorotnikova, Y. A. Vorotnikov, A. A. Ryadun, N. V. Kuratieva, K. V. Kozyr, N. R. Obedinskaya, E. I. Kretov, I. N. Novozhilov, Y. V. Mironov, D. V. Stass, O. A. Efremova and M. A. Shestopalov, *Dalton Trans.*, 2017, **46**, 11738–11747.

27 K. Kirakci, J. Zelenka, M. Rumlova, J. Martincik, M. Nikl, T. Ruml and K. Lang, *J. Mater. Chem. B*, 2018, **6**, 4301–4307.
28 L. Xiao, L. Gu, S. B. Howell and M. J. Sailor, *ACS Nano*, 2011, **5**, 3651–3659.
29 T. Sabri, P. D. Pawelek and J. A. Capobianco, *ACS Appl. Mater. Interfaces*, 2018, **10**, 26947–26953.
30 X. Zhang, L. Li, Q. Liu, Y. Wang, J. Yang, T. Qiu and G. Zhou, *J. Biomed. Nanotechnol.*, 2019, **15**, 184–195.
31 Q. Xu, X. Sun, F. Hu, R. Wan, V. Singh, P. Ma, J. Niu and J. Wang, *Materials*, 2017, **10**, 1173.
32 L. Vila-Nadal and L. Cronin, *Nat. Rev. Mater.*, 2017, **2**, 17054.
33 J. A. Burdick and K. S. Anseth, *Biomaterials*, 2002, **23**, 4315–4323.
34 R. Ruiz-Gonzalez, R. Bresoli-Obach, O. Gulias, M. Agut, H. Savoie, R. W. Boyle, S. Nonell and F. Giuntini, *Angew. Chem., Int. Ed.*, 2017, **56**, 2885–2888.
35 E. L. L. Yeo, J. U. J. Cheah, D. J. H. Neo, W. I. Goh, P. Kanchanawong, K. C. Soo, P. S. P. Thong and J. C. Y. Kah, *J. Mater. Chem. B*, 2017, **5**, 254–268.
36 M. M. Kim, A. A. Ghogare, A. Greer and T. C. Zhu, *Phys. Med. Biol.*, 2017, **62**, R1–R48.
37 C. Zhang, W. Bu, D. Ni, C. Zuo, C. Cheng, Q. Li, L. Zhang, Z. Wang and J. Shi, *J. Am. Chem. Soc.*, 2016, **138**, 8156–8164.
38 J. T. Robinson, S. M. Tabakman, Y. Y. Liang, H. L. Wang, H. S. Casalongue, D. Vinh and H. J. Dai, *J. Am. Chem. Soc.*, 2011, **133**, 6825–6831.
39 K. Yang, J. Wan, S. Zhang, B. Tian, Y. Zhang and Z. Liu, *Biomaterials*, 2012, **33**, 2206–2214.
40 K. Yang, L. Hu, X. Ma, S. Ye, L. Cheng, X. Shi, C. Li, Y. Li and Z. Liu, *Adv. Mater.*, 2012, **24**, 1868–1872.

